

Thin filaments in Hele-Shaw cells

Nitay Ben-Shachar, Michael C. Dallaston, and Scott W. McCue *

1 Introduction

Hele-Shaw cells consist of two parallel plates separated by a small gap. The discrepancy between the in-plate and out-of-plate length-scales gives viscous-dominated Poiseuille flow between the two plates. Averaging over the depth between the plates, the macroscopic in-plate dynamics are governed by the incompressible Darcy law,

$$\mathbf{u} = -\frac{b^2}{12\mu}\nabla p, \quad \nabla \cdot \mathbf{u} = 0, \quad (1)$$

where \mathbf{u} is the in-plate depth-averaged velocity, p is the pressure, b is the distance between the parallel plates and μ is the viscosity of the fluid [13, 11, 12]. Thus, Hele-Shaw flows mimic the behaviour of two-dimensional fluid flows in porous media.

Hele-Shaw flows have direct industrial uses, such as the application of adhesives [7]. Furthermore, they provide valuable insight to the governing dynamics of porous flows, which are typically in hard-to-access environments, such as the subsurface. Applications of subsurface, porous media flows include underground fluid mixing and CO₂ sequestration [10].

Nitay Ben-Schachar
School of Mathematics & Statistics, University of Melbourne
e-mail: nbenshachar@student.unimelb.edu.au

Michael C. Dallaston
School of Mathematical Sciences, Queensland University of Technology
e-mail: michael.dallaston@qut.edu.au

Scott W. McCue
School of Mathematical Sciences, Queensland University of Technology
e-mail: scott.mccue@qut.edu.au

* This report presents the results of a project undertaken by the first author at the Matrix Workshop *Instabilities in Porous Media*, April 3-23, 2024, under the supervision of the other authors.

Viscous fingering occurs in a Hele-Shaw cell when a viscous fluid is invaded by a less viscous fluid, as shown in Fig. 1. The interface between these fluids becomes unstable, and fingers form, grow and split. In contrast, when a viscous fluid invades a less viscous fluid, the interface is stable [13]. For the purposes of mathematical

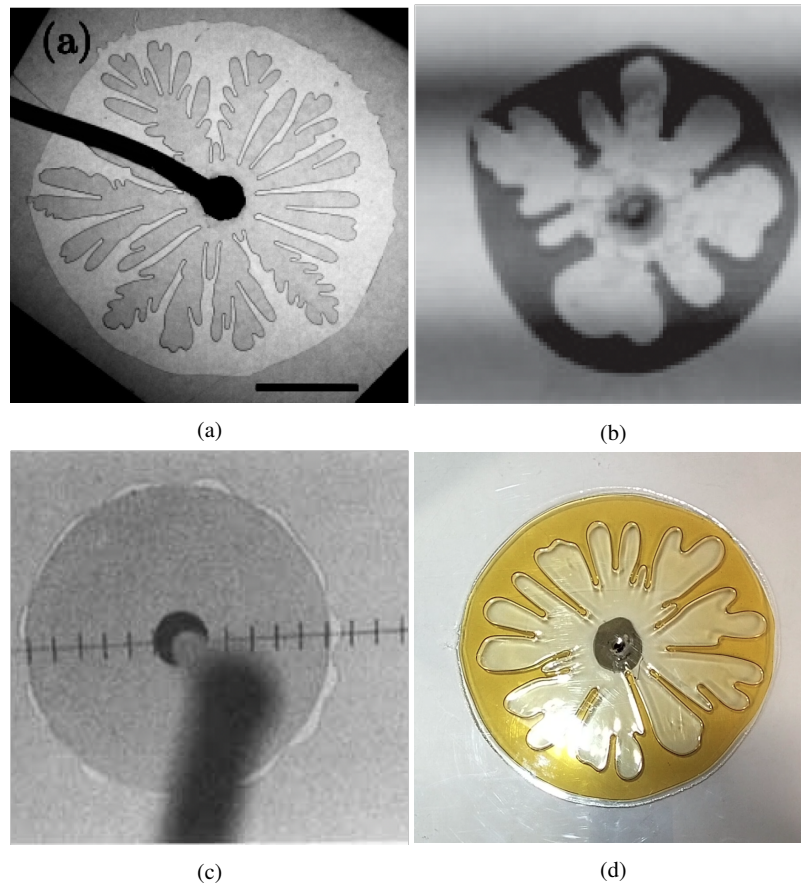


Fig. 1: Experiments of flows in a Hele-Shaw cell with multiple fluid interfaces; (a) Morrow et al. [11], (b) Ward and White [14], (c) Cardoso and Woods [2], (d) ‘home-made’ experiments with Emily Chen.

modelling, it is often assumed that the more viscous fluid is infinite in its extent, such as shown in Fig. 2a, with a single interface dividing the two fluids. However, flows in real Hele-Shaw cells typically exhibit multiple fluid interfaces [2, 11]; see Fig. 1. Therefore, for real Hele-Shaw experiments a more realistic model has two interfaces, such as shown in Fig. 2b. Morrow et al. [11] demonstrated, by studying the injection of air into a finite amount of water in a Hele-Shaw cell, that both inner

and outer interfaces can become unstable. When the distance between the inner and outer interfaces is comparable to the Hele-Shaw cell gap, the depth-averaged model fails and the two interfaces may merge (i.e., the inner air bubble bursts the fluid annulus).

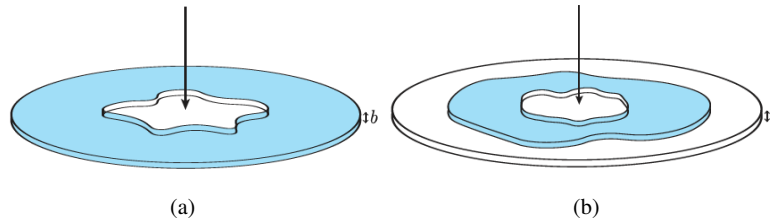


Fig. 2: Reprinted from Morrow et al. [11]. (a) Injection of a bubble (white) into an infinite expanse of a viscous fluid (cyan) in a Hele-Shaw cell. (b) Fluid annulus (cyan) expanding or contracting due to a maintained pressure difference between the inside bubble and the ambient air.

Recently, Dallaston et al. [4] developed general theory for the evolution of thin liquid filaments in Hele-Shaw cells, whereby the two interfaces are very close together. Here, the thickness of the liquid filament is much smaller than the radius of curvature of either interface, but significantly thicker than the Hele-Shaw cell gap such that the depth-averaged model applies. It was found that, in the absence of a bursting criteria (i.e., for an infinitesimally small Hele-Shaw cell gap), perturbations to straight, thin filaments grow into circular-like shapes, as can be seen in Fig. 3. However, these circular filament shapes have only been observed numerically, and their dynamics and stability are currently unknown analytically. Further, the shrinking filament thickness induces numerical instabilities for later times, making it difficult to glean the driving mechanism for the dynamics of these filament structures.

In Sect. 2 we summarise the general Hele-Shaw model [11] and the filament model from Dallaston et al. [4]. These are used to determine axisymmetric annular fluid solutions and to study their stability in Sect. 3. In Sect. 4 we derive a growing and translating solution to the filament model, describing the circle-like structures observed in numerical solutions. Conclusions and future work are discussed in Sect. 5.

2 Model outline

Consider the flow of a finite volume of fluid in a Hele-Shaw cell. We non-dimensionalise all variables by selecting the following scales:

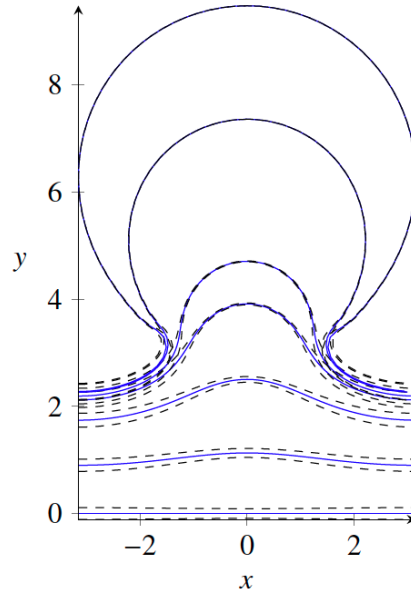


Fig. 3: Reprinted from Dallaston et al. [4]. Evolution of a perturbed straight filament, driven by a constant pressure gradient. An instability results in the interface stretching and thinning, until ultimately it appears that the filament approaches a circular shape. The blue line marks the centre of the filament, with the dashed black lines indicating the filament boundaries.

$$x_s = \frac{l}{2\pi}, \quad p_s = \frac{12\mu x_s}{b^2 t_s}, \quad (2)$$

where x_s is the spatial scale, p_s is the pressure scale, l is some macroscopic length of the fluid shape that will be chosen later, and t_s is an arbitrary timescale.

2.1 Full Hele-Shaw model

We consider the dynamics of an annular section of liquid, confined by air (i.e. inviscid fluid) on both the interior and exterior boundaries, see Fig. 2 [4, 11]. Scaling the governing equations, (1), gives

$$\nabla^2 p = 0, \quad \mathbf{x} \in \Omega, \quad (3a)$$

$$v_n = -\nabla p \cdot \hat{\mathbf{n}}, \quad \mathbf{x} \in \partial\Omega, \quad (3b)$$

$$p = \Delta P - \sigma \kappa, \quad \mathbf{x} \in \partial\Omega_{\text{in}}, \quad (3c)$$

$$p = \sigma \kappa, \quad \mathbf{x} \in \partial\Omega_{\text{out}}, \quad (3d)$$

where we have invoked appropriate pressure-jump conditions at the inner and outer interfaces, ΔP is the scaled driving pressure difference across the annulus, $\sigma = \hat{\gamma}/(p_s x_s)$ is the scaled surface tension, v_n is the boundary-normal velocity, $\hat{\mathbf{n}}$ is the unit boundary normal, and κ is the curvature of the boundary. The inner and outer boundaries are $\partial\Omega_{\text{in}}$ and $\partial\Omega_{\text{out}}$, respectively, while the fluid domain is Ω . With an appropriate choice for the timescale, t_s , either of ΔP or σ (if nonzero) could be scaled to unity. However, we retain both parameters explicitly to aid in interpreting the terms that arise in our analysis.

Other models of multi-layer radial Hele-Shaw flows have been proposed and studied, for example in [1, 3, 5, 9, 8, 15]. Gin and Daripa [8, 9] studied the linear stability of radial multi-layer Hele-Shaw cells, while Anjos and Li [1] used weakly-nonlinear stability analysis to predict the morphology of the viscous fingers that form. Zero-surface-tension models were considered by Crowdy and Tanveer [3], and Dallaston and McCue [5], where exact solutions were found through use of complex variable techniques. Zhao et al. [15] considered a radial three-layer Hele-Shaw system, with the outer fluid more viscous than the middle fluid, which in turn is more viscous than the inner fluid. The model described by Morrow et al. [11] and presented here, where a viscous fluid is confined on both inner and outer boundaries by an inviscid fluid, complements the work of Zhao et al. [15].

2.2 Filament model

The filament model applies when the distance between the outer and inner surfaces (the film thickness, h) is small compared to the radius of curvature of either interface. The film thickness is assumed to be significantly larger than the plate separation, b , such that the depth-averaged Hele-Shaw model is valid. In this limit, (3a)–(3d) can be approximated with a lubrication-style method, giving explicit equations for the evolution of the filament centreline and the thickness of the filament along the centreline, summarised below in Sect. 2.2.1. Resolving the governing equations to first-order in the lubrication parameter yields the so-called ‘full filament model’. However, the key model features can be captured by neglecting many of the derived terms, resulting in the reduced ‘regularised leading-order filament model’. As we will see in Sect. 3.2.2, the regularised leading-order filament model qualitatively agrees with the full Hele-Shaw calculations, (3a)–(3d), and allows for physical interpretation of the model predictions.

2.2.1 Full filament model

The full filament model is derived by Dallaston et al. [4] as

$$v_n = v_0 + \left(\frac{2h^2 \kappa^2 v_0 - h^2 v_{0ss}}{12} - \frac{hh_s v_{0s}}{4} + \frac{2\sigma \kappa_2}{h} \right), \quad (4a)$$

$$\frac{Dh}{Dt} = \kappa h v_n - \frac{\partial}{\partial s} \left[-\frac{h^3 \kappa_s v_0}{12} - \frac{h^2 h_s \kappa v_0}{4} + \sigma h \kappa_{1s} \right], \quad (4b)$$

with

$$v_0 = \frac{\Delta P + 2\sigma \kappa}{h}, \quad (5a)$$

$$\kappa_1 = \frac{h\kappa^2}{2} + \frac{h_{ss}}{2}, \quad (5b)$$

$$\kappa_2 = \frac{h^2 \kappa^3}{4} + \frac{hh_s \kappa_s}{4} + \frac{hh_{ss} \kappa}{2} + \frac{h_s^2 \kappa}{8}, \quad (5c)$$

where κ is the curvature of the centreline, s is the arclength variable parameterising the centreline, and D/Dt is a time derivative along the normal direction to the filament centreline. The first terms on the right hand side of (4a) and (4b) are the leading-order solutions in the lubrication approximation, while the remainder of the terms arise from continuing the expansion to first order in the lubrication parameter.

2.2.2 Regularised leading-order filament model

The regularised leading-order model is obtained by neglecting all terms of order the lubrication parameter in (4a) and (4b) except for the regularising term, $\sigma(hh_{sss})_s/2$, giving

$$v_n = v_0, \quad (6a)$$

$$\frac{Dh}{Dt} = \kappa h v_n - \frac{\sigma}{2} \frac{\partial}{\partial s} (hh_{sss}). \quad (6b)$$

The necessity of retaining the regularising term will be discussed further in Sect. 3.2.2. When surface tension is neglected from (6a) and (6b), the zero-surface-tension filament model of Farmer and Howison [6] is obtained.

3 Linear stability analysis of the annulus

Here we consider the linear stability of an annulus of fluid in a Hele-Shaw cell driven by a constant pressure difference between the inside and outside interfaces.

We will begin by considering an annulus of arbitrary thickness, followed by detailed analysis of the thin annulus where the filament model applies.

3.1 Full Hele-Shaw model

Parameterising the inner and outer fluid interfaces with a polar angle, θ , the curvature of each boundary is

$$\kappa_i = \frac{2(R_i')^2 - R_i R_i'' + R_i^2}{(R_i^2 + (R_i')^2)^{3/2}}, \quad (7)$$

where $R_I(t, \theta)$ and $R_O(t, \theta)$ are the radial locations of the inner and outer boundaries, respectively, $i \in \{I, O\}$ and the prime symbol, $'$, denotes differentiation with respect to θ . The boundary unit normal, pointing into the fluid domain, is

$$\hat{\mathbf{n}} = \pm \frac{\hat{r} - \hat{\theta}(R_i'/R_i)}{\sqrt{1 + (R_i'/R_i)^2}}, \quad (8)$$

where the positive and negative signs are taken for the inner and outer boundaries, respectively.

3.1.1 Base state - axisymmetric solution

The base, axisymmetric solution to (3a)–(3d), denoted with a subscript ‘ b ’, satisfies

$$\frac{d^2 p_b}{dr^2} + \frac{1}{r} \frac{dp_b}{dr} = 0, \quad (9a)$$

$$p_b(R_{bl}) = \Delta P - \frac{\sigma}{R_{bl}}, \quad (9b)$$

$$p_b(R_{bo}) = \frac{\sigma}{R_{bo}}, \quad (9c)$$

$$\frac{dR_{bl}}{dt} = - \left. \frac{dp_b}{dr} \right|_{r=R_{bl}}, \quad (9d)$$

$$\frac{dR_{bo}}{dt} = - \left. \frac{dp_b}{dr} \right|_{r=R_{bo}}. \quad (9e)$$

Solving (9a)–(9c) furnishes the pressure within the fluid,

$$p = \frac{1}{R_{bo}} + \left[\frac{\Delta P - \sigma(R_{bo}^{-1} + R_{bl}^{-1})}{\log(R_{bl}/R_{bo})} \right] \log\left(\frac{r}{R_{bo}}\right). \quad (10)$$

Substituting (10) into (9d) and (9e) gives the evolution equations for the inner and outer interfaces [11],

$$\frac{dR_{bl}}{dt} = \frac{\Delta P - \sigma(R_{bo}^{-1} + R_{bl}^{-1})}{R_{bl} \log(R_{bo}/R_{bl})}, \quad (11a)$$

$$\frac{dR_{bo}}{dt} = \frac{\Delta P - \sigma(R_{bo}^{-1} + R_{bl}^{-1})}{R_{bo} \log(R_{bo}/R_{bl})}. \quad (11b)$$

Equations (11a) and (11b) reveal a competition between the applied pressure difference between the inner and outer regions of the annulus (pushing the interfaces away from the origin), and the surface tension (pulling the interfaces toward the origin). The axisymmetric solution grows if $\Delta P > \sigma(R_{bl}^{-1} + R_{bo}^{-1})$, and shrinks if the inequality is reversed.

3.1.2 Linear perturbation

We now turn to the linear stability of the base solution derived in Sect. (3.1.1). The solution is written as a sum of the base solution and a small perturbation (subscript ‘ p ’),

$$p = p_b(r, t) + \varepsilon p_p(r, \theta, t), \quad (12a)$$

$$R_O = R_{bo}(t) + \varepsilon R_{pO}(t) \cos(n\theta), \quad (12b)$$

$$R_I = R_{bl}(t) + \varepsilon R_{pI}(t) \cos(n\theta), \quad (12c)$$

and ε is the small perturbation amplitude. Substituting (12a)–(12c) into (3a)–(3d), expanding for $\varepsilon \ll 1$ and collecting powers of ε , the governing equations and boundary conditions at $O(\varepsilon)$ are

$$\frac{\partial^2 p_p}{\partial r^2} + \frac{1}{r} \frac{\partial p_p}{\partial r} + \frac{1}{r^2} \frac{\partial^2 p_p}{\partial \theta^2} = 0, \quad (13a)$$

$$p_p(r_I, \theta, t) = -R_{pI} \frac{dR_{bl}}{dt} + \sigma \frac{R_{pI}(1-n^2)}{R_{bl}^2}, \quad (13b)$$

$$p_p(r_O, \theta, t) = -R_{pO} \frac{dR_{bo}}{dt} - \sigma \frac{R_{pO}(1-n^2)}{R_{bo}^2}, \quad (13c)$$

$$\frac{dR_{pI}}{dt} = - \left. \frac{\partial p_p}{\partial r} \right|_{r=R_{bl}} - R_{pI} \left. \frac{d^2 p_b}{dr^2} \right|_{r=R_{bl}}, \quad (13d)$$

$$\frac{dR_{pO}}{dt} = - \left. \frac{\partial p_p}{\partial r} \right|_{r=R_{bo}} - R_{pO} \left. \frac{d^2 p_b}{dr^2} \right|_{r=R_{bo}}. \quad (13e)$$

Solving these, we obtain the evolution equations for R_{pI} and R_{pO} ,

$$\begin{aligned} \frac{dR_{pI}}{dt} = & \left[\frac{1}{R_{bl}} \left(\frac{n(R_{bl}^{2n} + R_{bO}^{2n})}{R_{bO}^{2n} - R_{bl}^{2n}} - 1 \right) \frac{dR_{bl}}{dt} - \sigma \frac{n(n^2 - 1)(R_{bl}^{2n} + R_{bO}^{2n})}{R_{bl}^3(R_{bO}^{2n} - R_{bl}^{2n})} \right] R_{pI} \\ & - \frac{2nR_{bl}^n R_{bO}^n}{R_{bO}^{2n} - R_{bl}^{2n}} \left[\frac{1}{R_{bO}} \frac{dR_{bl}}{dt} + \sigma \frac{n^2 - 1}{R_{bl} R_{bO}^2} \right] R_{pO}, \end{aligned} \quad (14a)$$

$$\begin{aligned} \frac{dR_{pO}}{dt} = & \left[-\frac{1}{R_{bO}} \left(\frac{n(R_{bl}^{2n} + R_{bO}^{2n})}{R_{bO}^{2n} - R_{bl}^{2n}} + 1 \right) \frac{dR_{bO}}{dt} - \sigma \frac{n(n^2 - 1)(R_{bl}^{2n} + R_{bO}^{2n})}{R_{bO}^3(R_{bO}^{2n} - R_{bl}^{2n})} \right] R_{pO} \\ & + \frac{2nR_{bl}^n R_{bO}^n}{R_{bO}^{2n} - R_{bl}^{2n}} \left[\frac{1}{R_{bl}} \frac{dR_{bO}}{dt} - \sigma \frac{n^2 - 1}{R_{bO} R_{bl}^2} \right] R_{pI}. \end{aligned} \quad (14b)$$

These are identical to the results reported by Morrow et al. [11]. While difficult to interpret, (14a) and (14b) will be used as a benchmark for the filament model, which will be analysed next.

3.2 Linear stability of the filament model

We now turn to the regularised leading-order filament model derived by Dallaston et al. [4], summarised in Sect. 2.2.2.

3.2.1 Base state - axisymmetric solution

As in Sect. 3.1, the base state, denoted subscript b , is found by searching for axisymmetric solutions of the governing equations (6a) and (6b), i.e., where the centreline radius and filament thickness are arc-length independent. The axisymmetric solution satisfies

$$\frac{dR_b}{dt} = \frac{\Delta P - 2\sigma/R_b}{h_b}, \quad (15a)$$

$$\frac{dh_b}{dt} = -\frac{h_b}{R_b} \frac{dR_b}{dt}, \quad (15b)$$

where R_b is the centreline radius of the axisymmetric (base) solution. Taking the ratio of (15a) and (15b) and integrating with respect to time, we find the standard conservation of volume condition:

$$h_b(t)R_b(t) = h_b(0)R_b(0) = \frac{A}{2\pi}, \quad (16)$$

where A is the dimensionless surface area of the filament. Substituting (16) into (15a) and (15b) and integrating furnishes the centreline radius and film thickness solutions, respectively:

$$R_b(t) = \left(R_b(0) - \frac{2\sigma}{\Delta P} \right) \exp\left(\frac{2\pi\Delta Pt}{A} \right) + \frac{2\sigma}{\Delta P}, \quad (17a)$$

$$h_b(t) = \frac{h_b(0)R_b(0)}{(R_b(0) - 2\sigma/\Delta P) \exp(2\pi\Delta Pt/A) + 2\sigma/\Delta P}. \quad (17b)$$

As observed in the full filament model (Sect. 3.1), the axisymmetric solution is characterised by a competition between the applied pressure difference and the surface tension. The filament radius grows if the initial radius exceeds the critical radius R_c :

$$R > R_c = \frac{2\sigma}{\Delta P}, \quad (18)$$

and shrinks if the inequality is reversed. The growing filament radius increases exponentially, due to the shrinking thickness of the filament. In contrast, a filament whose radius shrinks becomes thicker exponentially. As such, the filament model will eventually become inapplicable for a shrinking filament, when its thickness becomes comparable to its radius.

3.2.2 Linear perturbation

Consider a linear perturbation of the annular filament solution derived in the previous section. We write the radius and thickness of the filament as

$$R(t, \theta) = R_b(t) + \varepsilon R_p(t) \cos(n\theta), \quad (19a)$$

$$h(t, \theta) = h_b(t) + \varepsilon h_p(t) \cos(n\theta). \quad (19b)$$

While we have assumed a restricted form for the linear perturbations, any desired filament perturbation can be obtained with an appropriate superposition of the perturbations, (19a) and (19b), with varying n . The chosen basis of the perturbations is shown in Fig. 4.

Substituting (19a) and (19b) into (6a) and (6b) and expanding to linear order for $\varepsilon \ll 1$, we obtain the governing equations for the perturbations of the film thickness and radius, respectively:

$$\frac{dh_p}{dt} = -R_p \frac{n^2 - 1}{R_b^2} \left(h_b \frac{dR_b}{dt} - \frac{2\sigma}{R_b} \right) - \frac{\sigma h_b n^4}{2R_b^4} h_p, \quad (20a)$$

$$\frac{dR_p}{dt} = -\frac{4\pi\sigma(n^2 - 1)}{AR_b} R_p - \frac{dR_b}{dt} \frac{1}{h_b} h_p. \quad (20b)$$

Using a ‘frozen time analysis’, the eigenvalues of the system described by (20a) and (20b) give the local growth rate of the perturbations h_p and R_p :

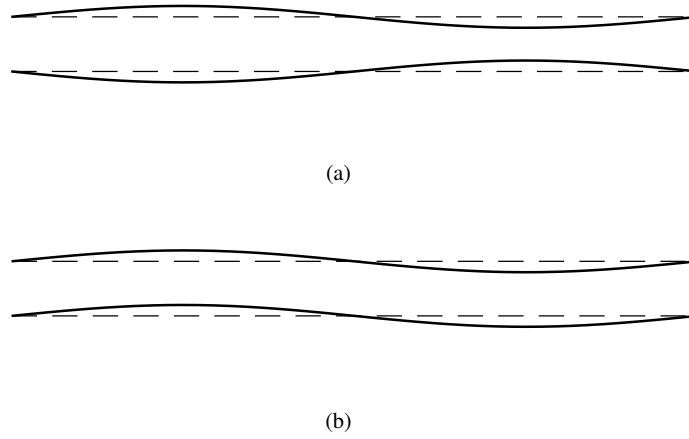


Fig. 4: Inner and outer interfaces of a filament perturbed from their equilibrium positions (dashed lines) for: (a) $h_p = 1, R_p = 0$, (b) $h_p = 0, R_p = 1$.

$$\lambda_{\pm} = - \left(\frac{An^4\sigma}{8\pi R_b^5} + \frac{2\pi(n^2-1)\sigma}{AR_b} \right) \pm \frac{1}{2} \left[\left(\frac{An^4\sigma}{4\pi R_b^5} + \frac{4\pi(n^2-1)\sigma}{AR_b} \right)^2 - \frac{4(n^2-1)}{R_b^2} \left(\frac{n^4\sigma^2}{R_b^4} - \frac{4\pi^2(R_b\Delta P - 4\sigma)(R_b\Delta P - 2\sigma)}{A^2} \right) \right]^{1/2}. \quad (21)$$

In the large radius limit, $R_b \rightarrow \infty$, (21) gives the limiting eigenvalues

$$\lambda_{\pm} = \pm \frac{\Delta P}{A} \sqrt{n^2 - 1} + O\left(\frac{1}{R_b}\right). \quad (22)$$

From (21) we find a critical mode number for stability,

$$n_c = \frac{R_b}{\sqrt{A\sigma}} \left((R_b\Delta P - 4\sigma)(R_b\Delta P - 2\sigma) \right)^{1/4}. \quad (23)$$

When $n_c > 1$, all wavenumbers satisfying $1 < n < n_c$ are unstable, while those satisfying $n > n_c$ are stable. Hence, all wavenumbers are stable when

$$R_b < \frac{4\sigma}{\Delta P} = 2R_c. \quad (24)$$

In the absence of the regularising term in the leading-order filament model (i.e., neglecting all n^4 terms in (21)), the (non-regularised) leading-order filament model growth rates are

$$\lambda_{\pm}^{\text{LO}} = -\frac{2\pi\sigma(n^2 - 1) \pm 2\pi\sqrt{n^2 - 1}\sqrt{(R_b\Delta P - 4\sigma)(R_b\Delta P - 2\sigma) + (n^2 - 1)\sigma^2}}{AR_b}. \quad (25)$$

The growth rates predicted by the full Hele-Shaw model (calculated by numerically diagonalising (14a) and (14b)), regularised leading-order filament model (21), and (non-regularised) leading-order filament model (25), are shown in Fig. 5 for selected parameter values. The regularised leading-order filament model closely predicts the full Hele-Shaw model for the given parameter values. For small mode numbers n , these exhibit positive growth rates, indicating unstable modes. For mode numbers greater than a critical ‘cut-off’ mode number, given by (23) for the regularised leading-order model, the growth rates are negative, indicating stable modes. In contrast, the leading-order model does not have a cutoff mode number; all modes are either stable (if $R_b < 4\sigma/\Delta P$) or unstable (if $R_b > 4\sigma/\Delta P$).

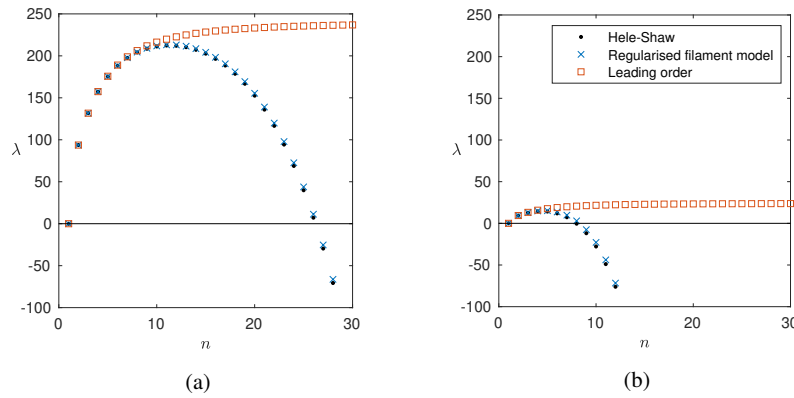


Fig. 5: Largest growth rate λ of perturbations from the annulus of given mode number n as predicted by the Hele-Shaw two-interface model, (14a) and (14b); regularised leading-order filament model, (21); and the (non-regularised) leading-order filament model, (25). The growth rates are shown for $\Delta P = 1, \sigma = 0.1, R_b = 1$ and (a) $h_b = 0.01$, (b) $h_b = 0.1$.

Next, we utilise the linear stability analysis to predict the perturbed filament dynamics. Initialising an annular filament with a perturbed centreline but constant thickness, composed of a random combination of the first 10 modes, we then numerically integrate (20a) and (20b) for the mode amplitudes. In Fig. 6 we compare the results of this analysis with a numerical solution to the full filament model, (4a) and (4b) [4].

At early times the integrated linear stability analysis matches the full filament model calculations. For the smaller annulus shown in Fig. 6, the mode amplitudes initially decay, before the amplitude of various modes grows when a critical radius

is reached. In contrast, for the larger annulus in Fig. 6, higher mode numbers dominate the centreline behaviour, as predicted by the linear stability analysis. The discrepancy between the integrated linear stability analysis and the full filament model increases with time, due to departure from the linear regime. However, the onset of fingering is well predicted by the linear theory, with the final centreline shape dominated by small ($n \lesssim 5$) and large ($n \gtrsim 5$) mode numbers, for Figs. 6a and 6b, respectively.

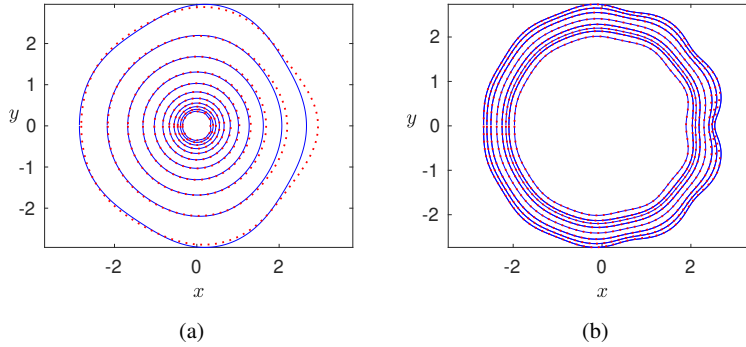


Fig. 6: Filament centrelines after a random perturbation of magnitude 1% to the centreline, shown at evenly spaced time intervals, as calculated using the full filament model (solid blue lines, (4a) and (4b)) and integrating the linear stability analysis (dotted red lines, (20a) and (20b)). Parameter values are $\Delta P = 1$, $\sigma = 0.1$, $h_b(0) = 0.05$, and (a) $R_b(0) = 0.35$, (b) $R_b(0) = 2$.

4 Pinned circles

As described in the previous section, an axisymmetric circular filament becomes unstable for sufficiently large radii, so that modes of perturbation grow for small time. However, for longer times the non-linear growth of these perturbations appears circular away from their attachment points to the remainder of the filament; see Fig. 7a. These dynamics share qualitative and quantitative features with the circular-like growth observed for perturbed flat filaments [4] (see Fig. 3): asymmetric radial growth, asymptoting to a circular geometry with a translating centre and increasing radius. These filament sections, henceforth referred to as ‘pinned circles’, appear stable for radii significantly larger than the critical stable radius of the axisymmetric filament. We thus search for non-axisymmetric solutions of the filament model that could describe these pinned circles.

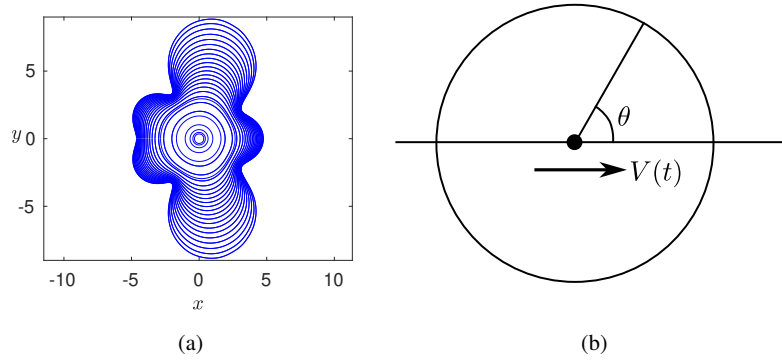


Fig. 7: (a) Centreline of the filament calculated by the full filament model, (4a) and (4b) [4], for $\Delta P = 1$, $\sigma = 0.1$, $h_b(0) = 0.05$ and $R_b(0) = 0.35$. The shown centrelines are unevenly spaced in time to show the expanding structure of the centreline. (b) Sketch of a ‘pinned circle’ whose centre translates with speed $V(t)$.

4.1 Approximate solution

The asymmetric growth of the pinned circles implies, from (4a), a non-constant filament thickness along the circle. We write (4a) and (4b) in polar coordinates whose origin translates with the pinned circle at velocity $V(t)\hat{x}$ (see Fig. 7b). Searching for circular solutions in the large radius limit, i.e., $R \gg 1$, in which the zero-surface-tension model is appropriate, the governing equations for the thickness, $h(\theta, t)$ and radius, $R(t)$, are

$$\frac{\partial h}{\partial t} = -\frac{\Delta P}{R} - \frac{\partial h}{\partial \theta} \frac{V(t) \sin \theta}{R}, \quad (26a)$$

$$\frac{dR}{dt} = \frac{\Delta P}{h} - V(t) \cos \theta. \quad (26b)$$

These are solved to give

$$V(t) = \frac{dR}{dt}, \quad (27a)$$

$$h(\theta, t) = \frac{\Delta P(t_0 - t)^2}{R(0)t_0(1 + \cos \theta)}, \quad (27b)$$

$$R(t) = \frac{R(0)t_0}{t_0 - t}, \quad (27c)$$

where t_0 is a parameter found from the initial conditions of the pinned circle.

In Fig. 8 the pinned circle asymptotic solution, (27b) and (27c), is compared with the nonlinear growth of the circular-like filament sections from numerical solutions

of the full filament model, (4a) and (4b), with an $n = 3$ perturbation to the centreline. The semi-major and semi-minor axes of the filament shape are computed by finding the points of maximal extent in the x and y directions (marked with a red circle and black squares, respectively, in Fig. 9). The distance between these and the centre of the pinned circle (marked with a green 'x' in Fig. 9) gives r_1 and r_2 plotted in Fig. 8b. The initial radius, $R(0)$, of the pinned circle model is fitted at the time corresponding to the black centreline in Fig. 8, giving a predicted blow-up time of $t_0 = 0.0154$ to three significant figures. The radius predicted by (27c) is plotted in Fig. 8b.

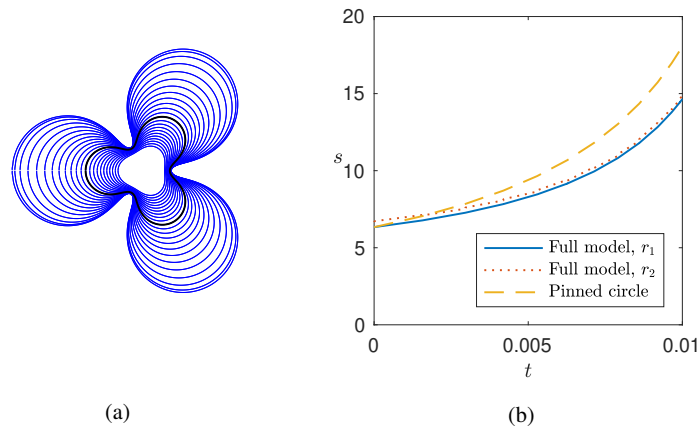


Fig. 8: (a) Numerical solution of the full filament model, (4a) and (4b), for $\Delta P = 1$, $\sigma = 0.5$ with an $n = 3$ perturbation to the centreline. (b) Semi-major and semi-minor axis (dotted red and solid blue lines, respectively) of the growing filament from the full model, compared with the predictions of the pinned circle analysis (dashed orange line, (27c)). The pinned circle model is fitted at the time corresponding to the centreline marked black in (a).

The filament away from its pinning point is not exactly circular, as seen by the unequal semi-major and semi-minor axis lengths. These lengths converge as the filament grows. The radius predicted by (27c) grows faster than the numerical solutions. Nonetheless, the qualitative behaviour of the filament's growth is captured by the pinned circle model. The numerical solution could not be run for longer time and larger radius due to the presence of numerical instabilities.

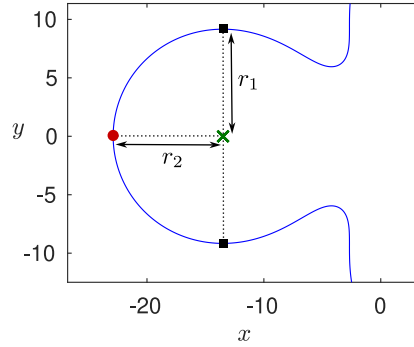


Fig. 9: Extraction of the semi-minor and semi-major axes lengths, r_1 and r_2 , respectively, from the identified points of maximal extent in the x and y directions of the circular-like filament section (blue line).

4.2 Properties of pinned circles

We highlight some of the properties of the pinned circles described by (27a)–(27c). As their name suggests, the circles are pinned at one end, i.e., the point at $\theta = \pi$ is fixed. The thickness of the filament diverges near the pinning point, and thus the model becomes inapplicable in the vicinity of $\theta = \pi$. Near these points the circular model does not describe the behaviour observed in the numerical solutions, due to the formation of ‘necks’ connecting the pinned circles, as seen in Figs. 7a and 8.

The total mass, $m(t, \alpha)$, i.e., area, between the angle range $-\alpha < \theta < \alpha$, is

$$m(t, \alpha) = 2\Delta P(t_0 - t) \tan\left(\frac{\alpha}{2}\right). \quad (28)$$

That is, any fixed angular section is losing mass over time! The liquid is ejected toward the pinning point, located at $\theta = \pi$, which encompasses all the mass in the limit $t \rightarrow t_0$. The pinned circle solution exhibits a finite time blow-up in the radius, at the time t_0 , in contrast to the exponential growth of the axisymmetric circles, described in Sect. 3.2. This is due to the mass-shedding toward the pinning point, decreasing the filament thickness and accelerating the radial growth.

5 Conclusion

Using the newly derived filament model of Dallaston et al. [4], the stability of fluid filaments in Hele-Shaw cells, driven by a constant pressure gradient, is studied. It is found that thin circular filaments grow if their initial radius exceeds the (dimensionless) critical radius, R_c (see (18)). Further, linear stability of the axisymmetric

solution reveals that all modes are stable for $R < 2R_c$, with modes becoming unstable for larger radii.

A translating circular solution is found for asymptotically large radius, termed a ‘pinned circle’. These are thought to describe the observed non-linear growth of filament into circular-like solutions. The solutions exhibit a finite-time blow up in the pinned circle radius, attributed to the circle shedding mass as it grows. Future work will include analysing the stability of the pinned circles, and their next-order corrections in the expansion of large radius.

References

1. Anjos, P.H.A., Li, S.: Weakly nonlinear analysis of the Saffman-Taylor problem in a radially spreading fluid annulus. *Phys. Rev. Fluids* **5**, 054,002 (2020). DOI 10.1103/PhysRevFluids.5.054002
2. Cardoso, S.S.S., Woods, A.W.: The formation of drops through viscous instability. *J. Fluid Mech.* **289**, 351–378 (1995). DOI 10.1017/S0022112095001364
3. Crowdy, D., Tanveer, S.: The effect of finiteness in the Saffman–Taylor viscous fingering problem. *J. Stat. Phys.* **114**(5), 1501–1536 (2004). DOI 10.1023/B:JOSS.0000013962.78542.33
4. Dallaston, M.C., Jackson, M.J.W., Morrow, L.C., McCue, S.W.: Two-interface and thin filament approximation in Hele–Shaw channel flow. *J. Fluid Mech.* **988**, A31 (2024). DOI 10.1017/jfm.2024.456
5. Dallaston, M.C., McCue, S.W.: New exact solutions for Hele-Shaw flow in doubly connected regions. *Phys. Fluids* **24**(5), 052,101 (2012). DOI 10.1063/1.4711274
6. Farmer, C., Howison, S.: The motion of a viscous filament in a porous medium or Hele–Shaw cell: a physical realisation of the Cauchy–Riemann equations. *Appl. Math. Lett.* **19**(4), 356–361 (2006). DOI <https://doi.org/10.1016/j.aml.2005.06.007>
7. Flaig, F., Fräger, T., Kaufmann, M., Vallée, T., Fricke, H., Müller, M.: How to find the perfect application pattern for adhesively bonded joints? *J. Adv. Join. Proc.* **8**, 100,147 (2023). DOI <https://doi.org/10.1016/j.jajp.2023.100147>
8. Gin, C., Daripa, P.: Stability results on radial porous media and Hele-Shaw flows with variable viscosity between two moving interfaces. *IMA J. Appl. Math.* **86**(2), 294–319 (2021). DOI 10.1093/imamat/hxab001
9. Gin, C., Daripa, P.: Time-dependent injection strategies for multilayer Hele-Shaw and porous media flows. *Phys. Rev. Fluids* **6**, 033,901 (2021). DOI 10.1103/PhysRevFluids.6.033901
10. Kampitsis, A.E., Kostorz, W.J., Muggeridge, A.H., Jackson, M.D.: The life span and dynamics of immiscible viscous fingering in rectilinear displacements. *Phys. Fluids* **33**(9), 096,608 (2021). DOI 10.1063/5.0064955
11. Morrow, L.C., De Cock, N., McCue, S.W.: Viscous fingering patterns for Hele-Shaw flow in a doubly connected geometry driven by a pressure differential or rotation. *Phys. Rev. Fluids* **8**, 014,001 (2023). DOI 10.1103/PhysRevFluids.8.014001
12. Morrow, L.C., Moroney, T.J., Dallaston, M.C., McCue, S.W.: A review of one-phase Hele-Shaw flows and a level-set method for nonstandard configurations. *ANZIAM J.* **63**(3), 269–307 (2021). DOI 10.1017/S144618112100033X
13. Paterson, L.: Radial fingering in a Hele Shaw cell. *J. Fluid Mec.* **113**, 513–529 (1981). DOI 10.1017/S0022112081003613
14. Ward, T., White, A.R.: Gas-driven displacement of a liquid in a partially filled radial Hele-Shaw cell. *Phys. Rev. E* **83**, 046,316 (2011). DOI 10.1103/PhysRevE.83.046316
15. Zhao, M., Anjos, P.H.A., Lowengrub, J., Li, S.: Pattern formation of the three-layer Saffman-Taylor problem in a radial Hele-Shaw cell. *Phys. Rev. Fluids* **5**, 124,005 (2020). DOI 10.1103/PhysRevFluids.5.124005